3

Isotropic wettability of natural Indian jujube (*Ziziphus mauritiana*) leaf surface and biomimicking

An overview of the subject content and mathematical tools relevant to our study has been discussed in chapter-2. This chapter addresses the structural morphology of Ziziphus leaf surface and isotropic wetting characteristics including static and dynamic aspects. Based on single level surface texture, the electrospining technique was employed for biomimicking using hydrophobic polymer solution to replicate micro-fibrous matted texture. Further, a mathematical model has been developed to predict wetting characteristics and structural pattern of the nonwoven fibrous surface texture.

3.1 Introduction

In this chapter, the unusual wettability aspect of the hairy, matted surface construct of the Indian jujube (*Ziziphus mauritiana*) abaxial leaf has been discussed. The isotropic wettability (see Appendix I, Fig. A.1(a)), where the three-phase contact line (TCL) is uniform, results in direction-independent wetting features [145, 146]. Bhushan *et al.* gave an account of hierarchical waxy structures: micro and nano dual textures which form the Cassie-Cassie wetting state of the lotus leaves being responsible for the unusual isotropic superhydrophobic wettability [38]. On the other hand, the surfaces of rose petals can attain isotropic superhydrophobicity with high surface adhesion due to a two-level surface texture: hierarchical micro papillae covered with a waxy nanotexture shown by the Wenzel-Cassie wetting state [40]. These leaf surfaces possess well-ordered, repetitive two-level nano-micro structures. However, a large class of leaf surfaces experiences a single-level surface micro-structure that can offer a remarkable superhydrophobicity owing to its amazing hairy matted texture. For example, plant leaves such as lady's mantle (*Alchemilla vulgaris L.*) [147], poplar leaf [89], ramee leaf [148], Chinese watermelon [148], silver ragwort

[88, 149, 150], etc. These hairy matted surfaces offer two important roles: first, the hairy leaf surface favours complete water roll-off with ensuing self-cleaning action, making contamination-free surfaces. Normally, these hairs are trichomes with unicellular, multicellular, or branched protrusions from the epidermal tissues. The hairs are biopolymer composites mainly composed of hemicelluloses, cellulose, and lignin [88, 151]. Second, the fibrous bottom surface provides strong protection against damage to leaf tissues caused by sunlight radiation. The proportion of incident sun radiation that is reflected from the upper (adaxial) part of leaves greatly depends on the bottom (abaxial) surface possessing a hairy matted texture [89, 152]. There are various methods to create patterned and textured surfaces, such as chemical etching [153, 154], gas plasma treatment [155], lithography [156], femtosecond laser patterning [157], irradiation [158], and electrospinning [69]. The choice of technique depends on the desired surface structure and complexity. Among these, electrospinning is particularly suitable for producing a hairy, matted surface texture.

This work reveals that the adaxial leaf part is hydrophilic in nature, while the abaxial surface exhibits superhydrophobic wetting due to the fibrous matted surface structure. Both superhydrophobicity and surface adhesion properties of tender, mature, and senescent leaf states have been discussed considering the role of the hairy matted texture. Moreover, by optimizing the electrospinning parameters, the electrospun-PVDF nonwoven, fibrous matted structures have been fabricated in an attempt to biomimic the abaxial *ziziphus* leaf texture. Finally, the worm-like chain (WLC) model [159] was introduced to explain the growth and spread of nonwoven fiber networks developed through artificial means.

3.2 Theory and model

3.2.1 Wettability of nonwoven fibrous matted surface texture

A model on nonwoven matted surfaces can be put forward to describe surface wettability. The wettability aspects of smooth solid surfaces is given in Young's Eq. (2.3), which is the relationship between three phase interfacial surface tension and CA. However, for the textured surface with air pockets can make the droplet be in the suspended wetting state, described by Cassie-Baxter model, shown in Eq. (2.11). Rewriting, Eqs. (2.3) and (2.11) as,

$$\cos\theta_a = \frac{\gamma_{SA} - \gamma_{SL}}{\gamma_{LA}}, \tag{3.1}$$

$$\cos\theta = f_1 \cos\theta_a - f_2, \tag{3.2}$$

where θ_a is the equilibrium advancing and θ is the Cassie-Baxter CAs, respectively. Numerous researchers have reviewed formulae and relations that describe wetting transition, from suspended (dewetting) to collapsed (wetting) state. Accordingly, transition occurs under many circumstances with factors like liquid droplet size, trapped air inside porous network, and liquid drop-air interface [160]. The entrapped air plays a major role to dictate the suspended state of the droplet. Giacomello *et al.* reported a continuum model for the wetting transition, as one moves from the Cassie to the Wenzel state as a function of the pressure across the interface [161]. Herein, the criterion is put forward for hydrophobic fibrous matted surface. In general, when a spherical water droplet of volume V and radius R_d comes in contact with the solid surface, it forms a spherical cap with water contact angle, θ and of height, h_c (<capillary length=$\sqrt{\frac{\gamma_{LA}}{\rho_w g}}$, g is the gravitational acceleration, ρ_w is water density) on fibrous matted surface as depicted in Figs. 3.1(a). Suppose there exist $2N_F$ fibers being randomly distributed over the x-y plane and that the spacing between each N_F pair of fibers is labelled as, $d_{i=1,2,3,...N_F}$. The side view of the droplet on irregular arrays of randomly separated fibers is shown in Fig. 3.1(b), whereas the magnified view of wetting curvature formed between two fibers is depicted in Fig. 3.1(c). If p_a is the atmospheric pressure outside the droplet, p_d is the Laplace pressure inside the droplet. Also, p_c, $p_{a'}$ are pressure inside curvature formed between fibers and pressure due to the entrapped air, respectively. Then, Young-Laplace pressure across the liquid curvature-air interface can be expressed by [162, 163],

$$p_c - p_{a'} = \frac{2\gamma_{LA}}{R_d} + p_a + \rho_w g h_c - p_{a'}. \tag{3.3}$$

Assuming the trapped air pressure between the fibers is equal to the pressure outside the droplet [164], we have

$$\Delta p = \frac{2\gamma_{LA}}{R_d} + \rho_w g h_c. \tag{3.4}$$

Considering the area under curvature as A_c, the pressure force, F_p, will be given by

$$F_p = \left(\frac{2\gamma_{LA}}{R_d} + \rho_w g R_d(1 - \cos\theta)\right) A_c. \tag{3.5}$$

To be mentioned, the pressure force across droplet curvature and trapped air interface is balanced by the vertical component of three-phase contact line surface tension force, as shown in Fig. 3.1(c). Now, suppose θ_a is the advancing contact angle on cylindrical fibers with length L, the trapped air-liquid interface curvature length L_a, and φ is the spreading angle as shown in Fig. 3.1(c), then the vertical component of surface tension force, $F_v = F\cos\delta$, will be given by,

$$F_v = 2L\gamma_{LA}\sin(\theta_a + \varphi - \pi). \tag{3.6}$$

These two forces compensate the position of curvature and result in spreading angle. Therefore, combining Eqs. (3.5) and (3.6) gives a relationship between spreading angle and water contact angle (WCA). At equilibrium,

$$\left(\frac{2\gamma_{LA}}{R_d} + \rho_w g R_d(1-\cos\theta)\right) A_c = 2L\gamma_{LA}\sin(\theta_a + \varphi - \pi), \tag{3.7}$$

or,

$$\theta_a + \varphi = \pi + \sin^{-1}\left(\frac{L_a}{2\gamma_{LA}}\left(\frac{2\gamma_{LA}}{R_d} + \rho_w g R_d(1-\cos\theta)\right)\right). \tag{3.8}$$

From Eqs. (3.4), (3.7), and (3.8), if the droplet curvature between two fibers undergoes zero hydrostatic pressure [164], i.e., $\Delta p = 0$, then the curvature becomes flat. Therefore,

$$\sin(\theta_a + \varphi - \pi) = 0, \tag{3.9}$$

or,

$$\theta_a + \varphi = \pi. \tag{3.10}$$

Considering fibers subjected to the above criterion, f_1 and f_2 can be expressed in terms of spreading angle, fiber radius, and average spacing between any pair of fibers given by,

$$f_1 = \frac{r\varphi}{r+D}, \tag{3.11}$$

$$f_2 = \frac{r(1-\sin\varphi)+D}{r+D}. \tag{3.12}$$

Using these in eq. (3.2), the modified Cassie-Baxter equation will be given by [164],

$$\cos\theta = \frac{r\varphi}{r+D}\cos\theta_a - \frac{r(1-\sin\varphi)+D}{r+D}. \tag{3.13}$$

Here, $2D$ is the average separation of randomly separated nonwoven matted fibers and given by,

$$D = \sum_{i=1}^{N_F} d_i P_i(\theta(l)), \tag{3.14}$$

where $P_i(\theta(l))$ is the normalized Gaussian probability distribution function (See Section 3.4.3). From Eqs. (3.10) and (3.13), one can say that the suspended state of the water droplet is more favourable when equilibrium advancing CA is greater than, or equal to $\pi/2$. As for the hydrophobic fibers, the collective response of fibers under

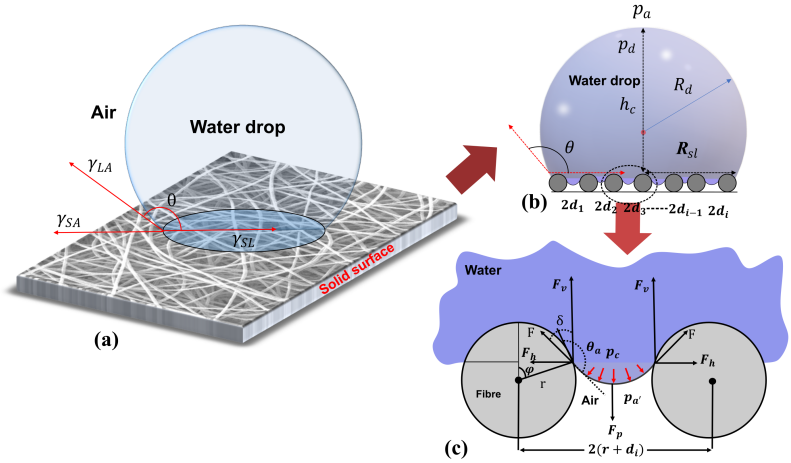

Figure 3.1: (a) Schematic diagram of wettability of water droplet on fibrous matted surface (not scale with the real experimental specimen). (b) Side views of a suspended water droplet on the cross-sectional irregular array of fibers with entrapped air within. (c) A magnified side view depicting a pair of fiber's cross section and liquid–air interface over the entrapped air gas.

wetted area (πR_{sl}^2) provides the suspended state of the spherical droplet with height h_c (Figs. 3.1(a) and 3.1(b)).

3.3 Experimental procedure

3.3.1 Sample collection and preparation

Fresh Indian jujube (*Ziziphus mauritiana*) leaves were gently collected from the decade old trees (available in our university campus) in the wee hour of morning. To retain the physiological state intact which might affect the surface texture, only a minimal time lag of less than an hour is kept between plucking of leaves and droplet characterization on the leaf surfaces. The three distinct states of *Ziziphus* leaves were chosen by visual appearance namely, tender, mature, and senescent states. The samples were placed in the glass petri dish carefully in ambient environment and air blown to remove away common particulate matter like mist, dust, pollen etc. The dimension (length x width) of the leaves from the tender to senescent states ranges, 4.7×2.5 cm^2 - 9.6×7.3 cm^2.

3.3.2 SEM imaging and water contact angle (WCA)

The surface morphologies of the *Ziziphus* leaves were captured on a scanning electron microscope (*JSM 6390LV, SEM*). As for SEM characterization, the sample was cut into 5×5 mm^2 and then, several nm platinum layers were deposited as per requirement. To prevent surface shrinkage, the leaf was secured to the holder of the platinum coater sputtering apparatus using acrylic double-sided adhesive tape, and

then 6-7 nm layers of platinum was deposited to make the surface conductive. After the Pt coating, the SEM analysis was made at different sites and with different magnifications. For characterization of wettability features, at least three specimens representing three distinct physiological states were taken and gently cut into 10 × 10 mm^2 pieces as per need. Generally, mid-regions with and without venation marks were selected from the leaf parts and then, affixed on the microscope glass slide with the help of a double-sided adhesive tape at opposite ends. The WCA measurements were carried out by employing sessile drop method using an advanced Contact Angle Meter setup (*Kyowa Interface Science®, Japan*) in our lab. For WCA and CAH characterization, droplets of size as low as 5 μL volume have been considered. In the experimental configuration for WCA measurements, micro-droplets were generated with the help of a syringe pump unit and then allowed to place gently on the specimen of interest (Fig. 3.2). The subsequent WCAs were determined by analysis of images captured on a high-speed camera and using a white light source. As for CAH analysis, the dynamic WCA measurement was conducted using a revolving specimen stage, rotated up to 90°.

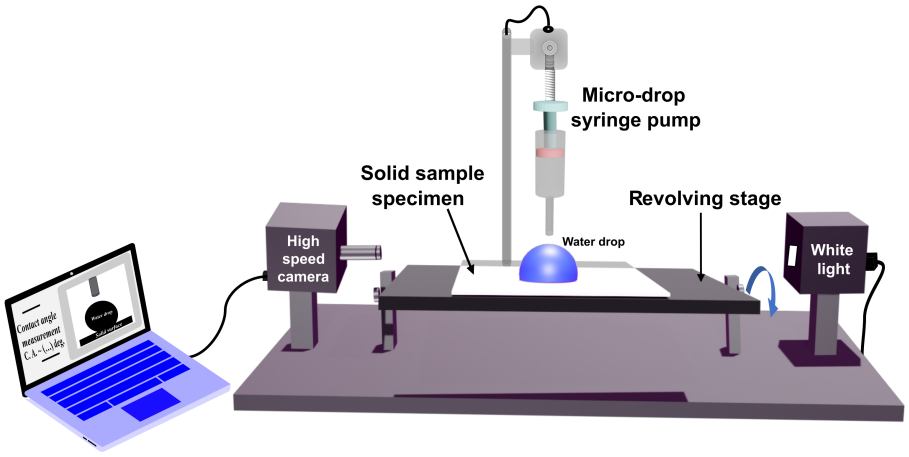

Figure 3.2: Schematic illustrating the experimental contact angle meter setup for measuring water contact angle.

3.4 Morphology of *Ziziphus* leaf surface and biomimicking

3.4.1 Natural adaxial and abaxial *Ziziphus* leaf surface

The appearance of tender and mature leaves present in the Indian jujube branch can be found in the optical images shown in Fig. 3.2(a). Whereas close-up views of the adaxial and abaxial surfaces are shown in Figs. 3.2 (b) and 3.2(c), respectively. As can be witnessed, the adaxial surface gives an oily-like dark green advent while the

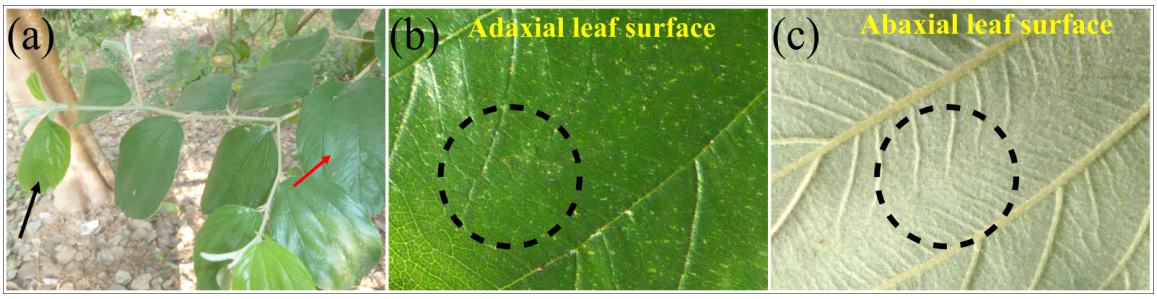

Figure 3.3: (a) Digital photograph of *Ziziphus mauritiana* branch depicting adaxial sides of leaves. The black and red arrows on leaves indicate tender and mature states; respectively. (b) and (c) show zoomed-in photographs of adaxial and abaxial leaf surfaces, respectively.

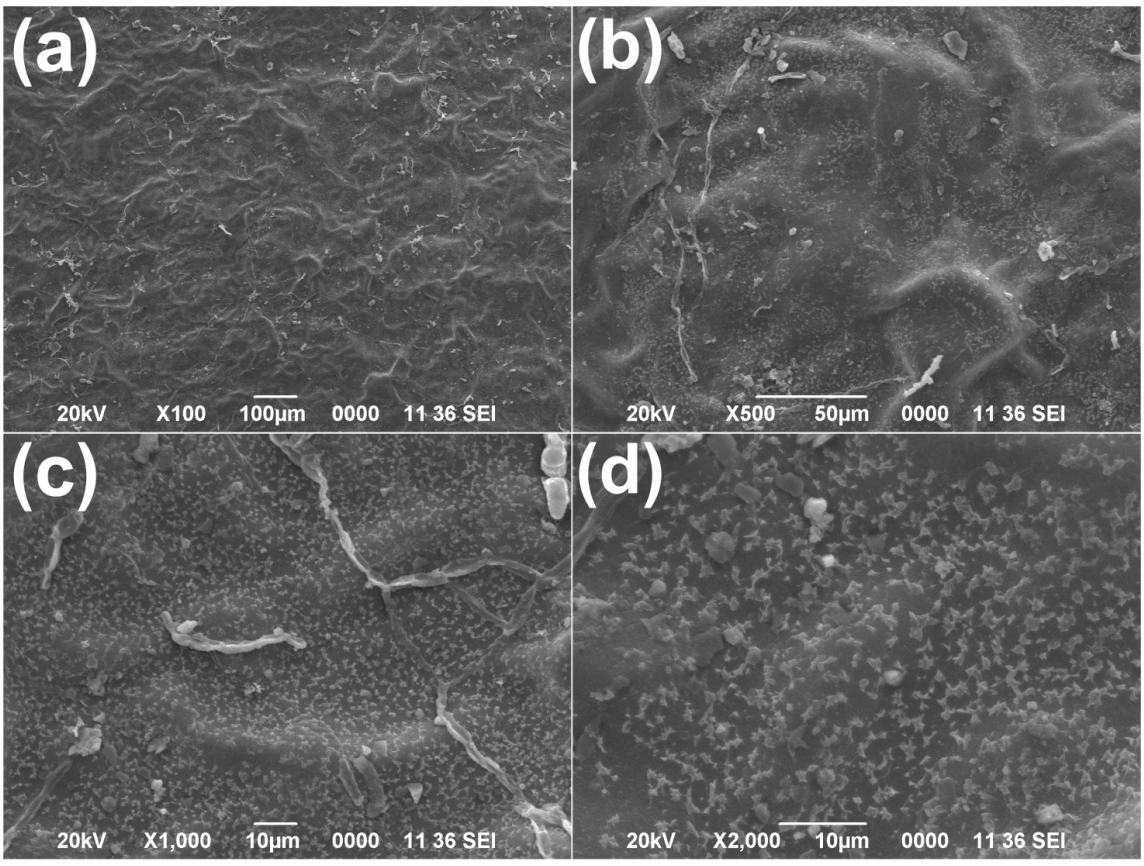

Figure 3.4: (a-d) SEM images of adaxial *Ziziphus* leaf surfaces at different magnifications. Folds and kinks on waxy epidermal region can be clearly seen.

abaxial side offers an off green-white appearance of the studied leaves. The dotted black circles essentially depict the sites chosen for leaf characterization.

The micrograph of the mature leaf surface of the adaxial part is depicted in Fig. 3.4 at different magnifications. Of particular interest, the micromorphological views of the abaxial tender, mature, and senescent states can be visualized from the SEM images shown in Fig. 3.5. The SEM images of the abaxial leaf specimens at different magnifications for the tender, mature, and senescent states are shown in Figs. 3.5(a-c), 3.5(d-f), and 3.5(g-i), respectively.

Interestingly, the adaxial leaf exhibits profoundly smooth surface feature while the

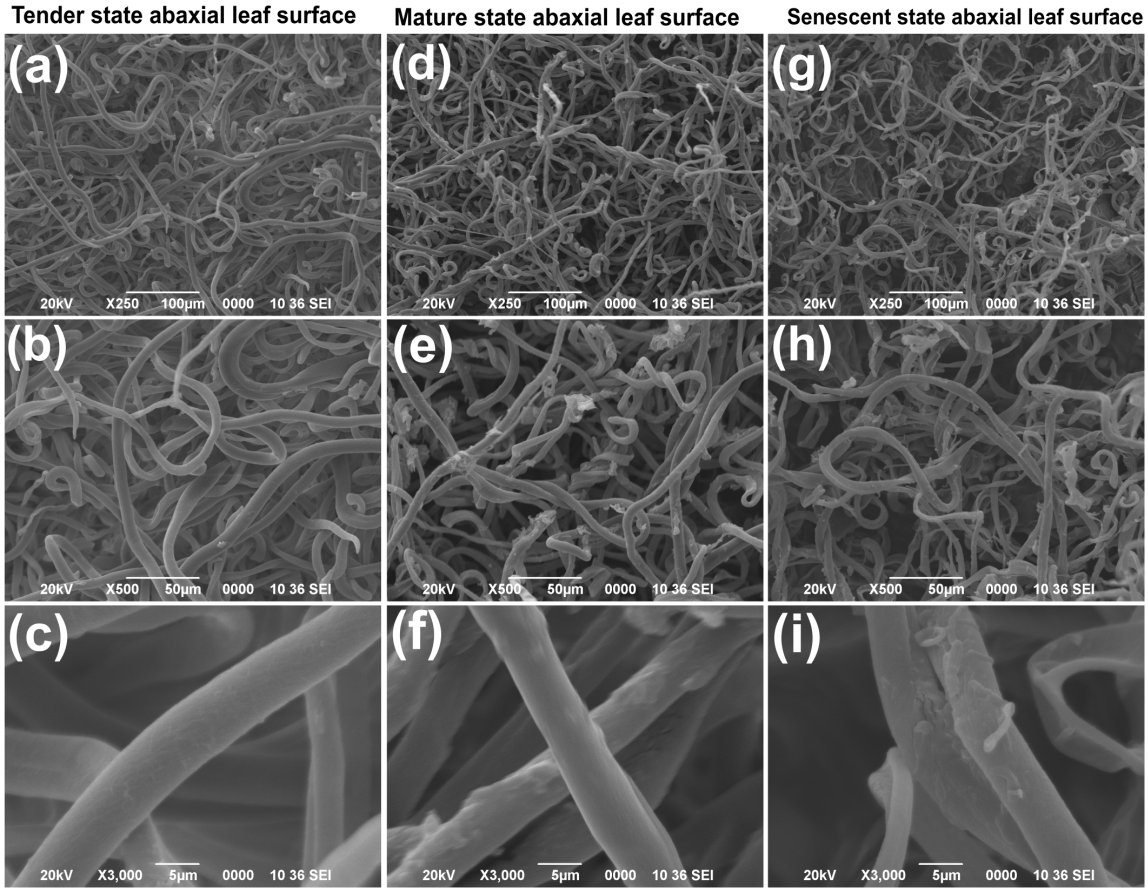

Figure 3.5: The SEM images of abaxial matted surface texture for the tender, mature, and senescent state *Ziziphus* leaves are shown in (a-c), (d-f), and (g-i), respectively.

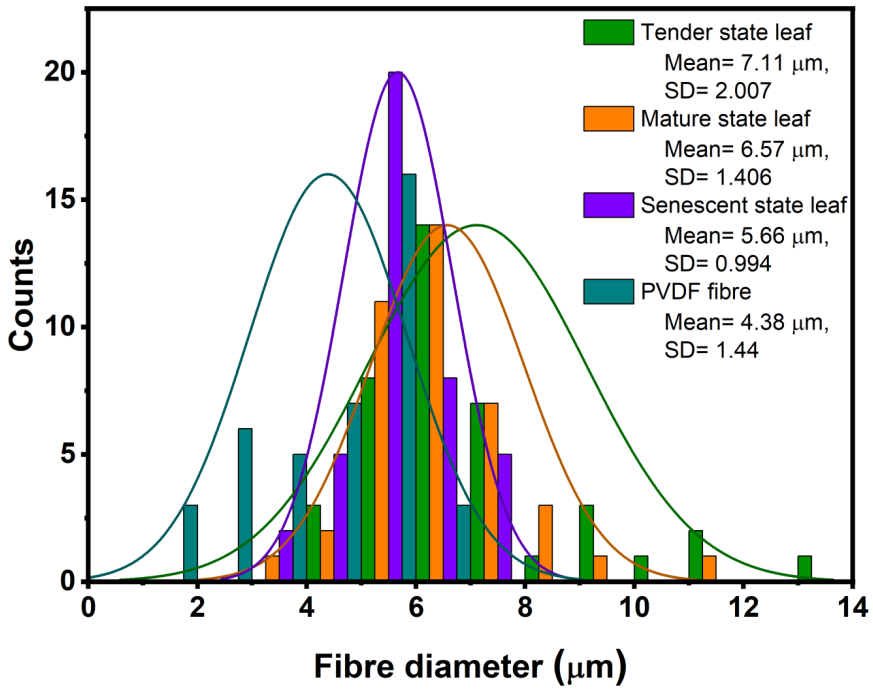

Figure 3.6: Statistical distribution on microfiber diameter of three states of abaxial leaf surface and PVDF matted surface by employing image analysis on SEM images.

abaxial surface seems to evolve with hairy matted network. The abaxial leaf surface is believed to be enriched with curved fibers, with a typical fiber diameter in the range of ~5.6 - 7.1 μm of different physiological states of *Ziziphus* leaves, Fig. 3.6. The arrangement of these non-woven fibers, together with varied diameters, will give rise to a porous network on the abaxial surface of the *Ziziphus* leaf. consequently, it favors the suspended state of wetting and consequently, superhydrophobicity. The non-woven, matted leaf surface with fibers in it was analysed segment-wise for determining porosity using *ImageJ software*® (*diameter-J* plugin) [165]. Interestingly, the tender leaf state has a porosity index in the range of ~49–55%, but mature and senescent states have relatively lower range values, e.g., ~42–49% and ~45–48%, respectively (see Appendix I, Fig. A.2). Relying on texture differences, surface wettability was examined and compared for distinct physiological states of *Ziziphus* leaves: tender, mature, and senescent specimens.

3.4.2 Biomimicking of *Ziziphus* microfibrous surface texture

Exhibiting hairy matted surface texture of microfibers, the SEM micrographs of tender, mature and senescent *Ziziphus* leaf states can be found in Fig. 3.5. To mimic hairy matted texture of *Ziziphus* abaxial leaf surface, we employed electro-spinning technique. To be mentioned, electrospinning technique is believed to be an ideal method to generate and cast fibers of varied dimensions and thus very appropriate to produce microfiber matted texture surface.

In the effort for biomimicking of matted surface construct, at first, PVDF pellets (PVDF, 99.9% pure, Merck®) were dissolved in a solution with 1:1 ratio of dimethylformamide (DMF, analytical standard, 98% pure) and acetone (analytical standard, 98% pure) to produce an appropriate polymer solution with a concentration of 21 wt%. The precursor sol was stirred homogeneously with a magnetic stirrer for 3 h and at a constant speed of ~750 rpm on a hot plate set to temperature ~ 60° C. With the help of electrospinning setup (*E-Spin Nanotech Pvt. Ltd., India*) under ambient room temperature and with relative humidity (RH) ~78%, and upon repetitive attempts, bead-free microfibers were drawn out of the PVDF precursor. The steps involved in biomimicking following electrospinning process are illustrated in Fig. 3.7.

In this regard, the prepared PVDF solution was loaded into a ~5 mL disposable syringe, which was mounted on the electrospinning apparatus. A high voltage, ranging from ~10 kV to 15 kV, was applied to the conductive needle tip (diameter of ~0.55 mm) of the syringe. The cylindrical collector was wrapped with 18 μm thick aluminum foil and positioned to receive the fibers. Initially, the collected fibers exhibited beaded microspheres with diameters of a few micrometers. This formation occurred under a specific solution concentration (10 wt%), with fixed spinning dis-

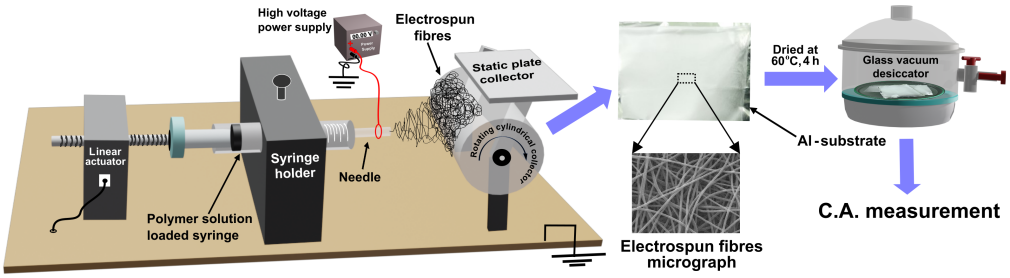

Figure 3.7: The schematic shows procedures of biomimicking using electrospinning unit.

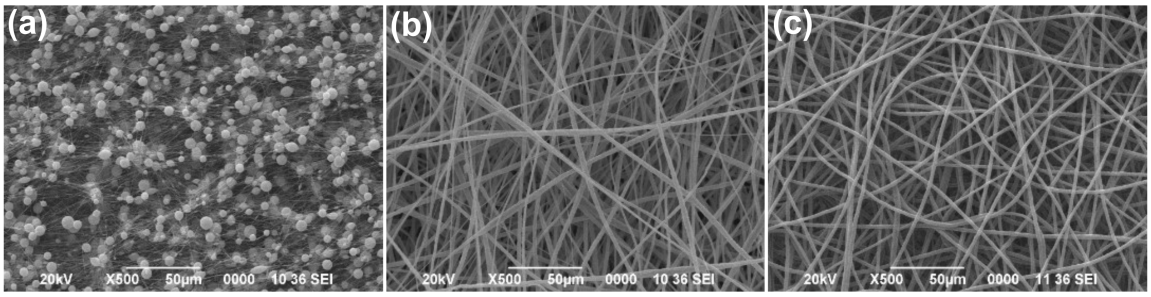

Figure 3.8: The SEM images (a-c) shown the scenarios before optimisation of the electrospun PVDF fibers with microsphere (beads), straight fiber, and non-woven microfibers produced at different solution concentrations, collector spinning speed, flow rate etc.

tance (∼10-15 cm), applied voltage (∼10-15 kV), collector rotation speed (∼200-800 rpm), and solution flow rate (∼4-6 mL/h), Fig. 3.8(a). As the solution concentration (and viscosity) increased from ∼10 wt% to 15 wt% and 21 wt%, partially straight, bead-free fibers were collected, as shown in Figs. 3.8(a) and 3.8(b).

Due to the complex texture of fibrous leaf surfaces, it was challenging to replicate them. Nevertheless, to achieve comparable morphology and diameters of fibrous matted leaf construct, numerous parameters were optimized in the electrospinning setup with static plate collector employed to develop the desired nonwoven fiber network. The flow rate of PVDF solution considered was 6 $mL.h^{-1}$, while distance between the static plate collectors to the needle head was set as, 10 cm. Under these circumstances, the deposition of microfibers was scheduled for about 1 h on the Al-substrate and subsequently, the hairy, matted film was dried at a temperature of $\sim 60^{\circ}$ C for 4 h. It is worth noting here that, comparable morphologies with tender state could be obtained at a solution concentration of 21 wt%. and displayed in Figs. 3.9(d-f). Although controllable biomimicking of irregular pattern is tedious, with accurate protocol and optimization hairy matted structures could be formed (see Appendix I). The diameter distribution of the electrospun PVDF fibers can be analysed on captured SEM image considering spatially nonwoven feature, shown in Fig. 3.9(e). Also, as grown PVDF matted texture surface porosity was estimated indirectly from the SEM image and found ∼49%. Not surprisingly, with varied and length of micro-fibers the average diameter is predicted as, ∼4.38 μm (Fig. 3.6).

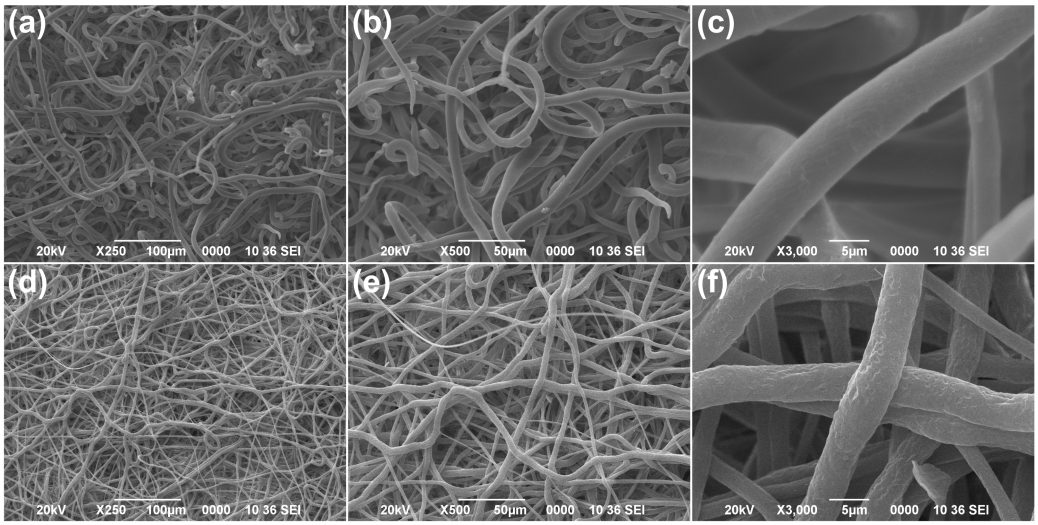

Figure 3.9: (a)–(c) depict SEM images of *Ziziphus* tender abaxial leaf surface with low and higher magnifications. Also, (d)–(f) show replicated, electrospun PVDF fibrous matted surface in proportionate magnifications. Note the curved nonwoven fibers at higher magnifications for (c) natural and (f) fabricated systems.

3.4.3 Worm-like chain model analogue for fibrous network

Finely knitted fibers/threads come with repetitive, periodic units which are easier to handle. The worm-like chain (WLC) model is a mathematical model commonly used to describe the behaviour of flexible polymer chains [166], such as fibers or polymers in a network. This model assumes that the chain can be approximated as a series of connected segments, resembling a series of worms connected in a chain. Therefore, the stochastic fiber network can be found by random-walk algorithms [167]. When applied to fibrous matted networks, the WLC model provides a simplified representation of the behaviour of the individual fibers within the network. The model accounts for the fibrous matted networks by producing representative volume elements (RVE) in the x-y plane.

Herein, we define a characteristic curved length scale known as the persistence length L_P [168]. Each fiber is built as a discrete jointed segment with length $l_S \ll L_P$. Each i-th segment makes a certain bending angle, θ, with respect to the $(i-1)$th segment as revealed in the schematic in Fig. 3.10(a). This is randomly drawn from the statistical distribution of the bend angle given by Gaussian distribution with zero mean and variance, given by $\sigma_\theta^2 = \frac{l_S}{L_P}$. Apparently, fiber shape is exclusively controlled by the persistence length. One of the most popular normal probability distribution functions is the Gaussian probability density function, which arises as a consequence of independent and identically distributed random variables summed together regardless of the shape of the original distribution. According to the WLC model, the two-dimensional normal probability density function correlation is given

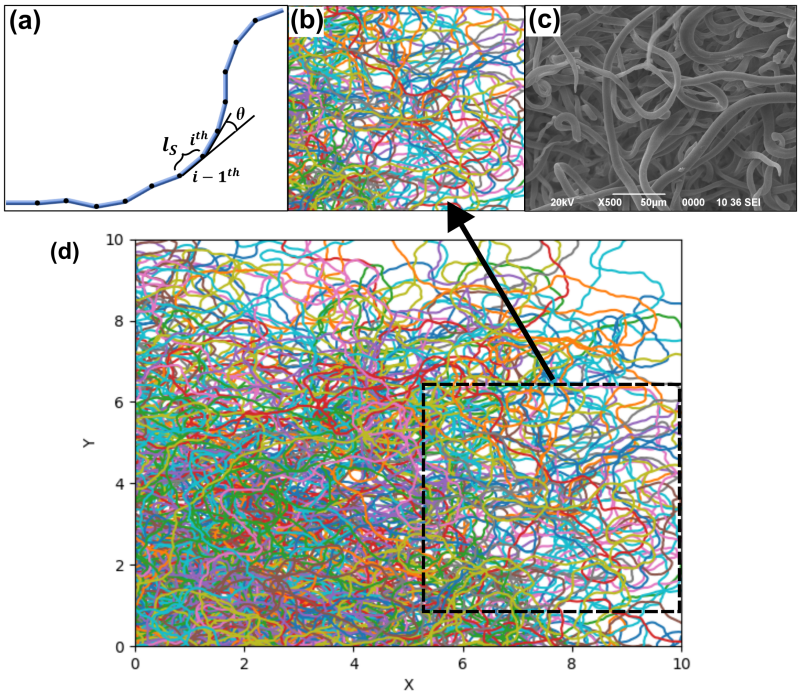

Figure 3.10: (a) Schematic presentation of stochastic, worm-like single fiber with jointed segments and associated parameters. An angle θ is made between tangents of two consecutive, ith and (i-*1*)th segments. (b) A sectional WLC model view of yarn-like microfibers generated using python 3.1 (*open source software*). Colors are being used to distinguish fibers, one from another. (c) SEM image of hairy, matted *Ziziphus* leaf surface texture. (d) The dashed region (X 5.5-10, Y 1-6.5) indicate snapshot provided in (b).

by [167],

$$P(\theta(l_S)) = \frac{1}{\sqrt{2\pi\sigma_\theta^2}} \exp\left(-\frac{\theta^2}{2\sigma_\theta^2}\right). \tag{3.15}$$

The Python code was considered to generate stochastic, nonwoven fiber shapes by random-walk algorithms using the above-described Gaussian distribution for random numerical values, depicted with a specific sectional view in Fig. 3.10(b) of Fig. 3.10(d). The distinct colour traces are representative fibers with yarn-like spread, bending, and crossing. To be noted, the density of chains is always higher at the origin than at its periphery. The structures grow in a radially outward direction to cover the whole space. At any instant of the iterative process, the structure is allowed to terminate in any two independent axes, without returning to the initial one. Therefore, any specific section of the whole area can certainly resemble any matted surface (including artificial ones derived under set experimental conditions) existing in nature. Here, such a replication scenario is found, as shown in Fig. 3.10(c).

The 2D WLC model provides a close analogy to the matted fibrous texture observed on the nonwoven *Ziziphus* surface. Consequently, the patterned surface textures of natural leaf specimens and artificially grown PVDF textures can be effectively interpreted using a global model like the WLC.

3.5 Contact angle characterization

3.5.1 Contact angle assessment and superhydrophobicity

Known as a routine technique, the water contact angle (CA) characterization of rough surfaces is crucial to validate its hydrophobicity feature. The tender state of the abaxial leaf comprises healthy fibers with an average diameter of ~7.11 μm and characterizes a superhydrophobic state, exhibiting a WCA as high as ~151.1° ± 2.5° (Fig. 3.11). The average diameter declines for mature and senescent states offering respective values of ~6.57 and ~5.67 μm (Fig. 3.6). The fibers present seem to contract and are under strain as one moves from the tender to the senescent leaf state. Accordingly, less healthy fibers account for the abaxial surface constructs, and the WCA falls to ~148° and 143.7°, eventually. Observably, the hydrophobicity of the senescent state abaxial leaf gets lowered compared to that of the tender and mature state abaxial leaf surfaces. Conversely, the adaxial surface of the tender leaf state has a hydrophilic feature and exhibits a WCA value of ~66.4° ± 0.9°. However, it increases up to ~75.9° ± 1.7° in the case of the adaxial surface of the senescent leaf. Under no circumstance and for any adaxial leaf state, the WCA could reach an obtuse angle (>90°). Nevertheless, the respective WCA of the mature leaf surface with adaxial and abaxial sides are ~73.5° ± 5.4° and ~147.1° ± 6.7°. To be specific, the abaxial matted surface possesses a superior dewetting feature compared with the greenly adaxial counterpart. Furthermore, when the mature leaf state attains the senescent state, the surface wettability of the abaxial matted leaf of the latter would get lowered by several degrees, ~143.7° ± 4.7°. Essentially, the presence of porosity on textured surfaces is responsible for creating a suspended state which favours the low wetting regime in the abaxial leaf surface. The tender leaf state has a large porosity index while mature and senescent states have relatively lower range values. The slightest alteration in the porosity index can cause enough change to the number of air voids or spaces that could be entrapped with air. Consequently, surfaces having relatively high trapped air voids will contribute largely to the suspended state and consequently, apparent superhydrophobic behaviour. The surface free energy (SFE) was estimated by the *Kaelble Uy model* [169], where liquid water and ethylene glycol were taken as the reference liquids (Fig. 3.11). According to the *Kaelble Uy model*, the total surface free energy of a solid surface can be given by the sum of polar and dispersive components due to independent interactions of solids and liquids [170]. The total SFE of the abaxial surface for the tender, mature, and senescent states were estimated to be ~0.843 mJ/m^2, ~0.947 mJ/m^2, and ~1.514 mJ/m^2, respectively (see Appendix I, table T.1).

The fabricated PVDF fibrous matted surface unveils a *Ziziphus* matched microstructure, measured WCA as high as ~145.7°. Yet, assigning to the replication of

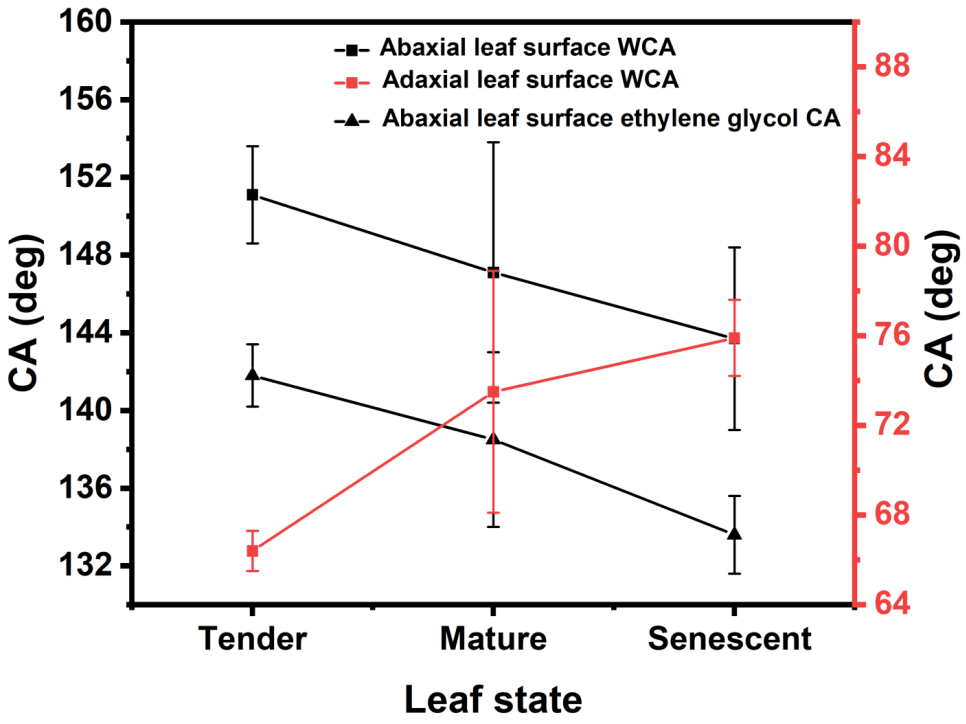

Figure 3.11: The plot of WCA and ethylene glycol CA of tender, mature, and senescent states of abaxial *Ziziphus* leaf surface (black), and WCA for the adaxial parts of three states (red).

the exact physiological state of the leaf texture was quite difficult. Qualitatively, the as-grown PVDF texture exhibits features similar to those of mature and senescent leaf surfaces with comparable porosity and superhydrophobicity characteristics but without any evidence of rolling off event. Nevertheless, in terms of morphological distribution, the PVDF surface shows a good resemblance with that of the tender leaf texture.

3.5.2 Contact angle hysteresis, roll-off, and superadhesion aspect

Recognized as a crucial adhesion parameter, contact angle hysteresis (CAH) is the difference between the maximum advancing and minimum receding angle experienced by the water droplet (see Sec:2.4.2, Fig. 2.6 (b)). Upon base slanting, the relationship between three phase contact line (TCL) motion and apparent WCA can help define the behaviour of the apparent advancing and receding CAs for the superhydrophobic textured surface. Apparently, the WCA is the time average between advancing (θ_A) and receding (θ_R) CAs. Physically, when a tilt is given to the solid base, the WCA increases linearly, and the droplet tends to bloat outward about the fixed TCL. In fact, the contact line remains pinned until the edge transition of apparent advancing contact angle shifts to a new location [171]. Whether the droplet will roll off or not will depend upon the pinning parameter, μ, and on the extent of base-tilting, α. The

pinning force, f_P, opposes the motion of the effective pinning length, l_e, of the TCL that arises due to gravitational force, and with a slanting angle α. Mathematically [172],

$$f_P = mg\sin\alpha = \mu l_e. \tag{3.16}$$

The effective pinning contact line length can be treated as the effective droplet boundary contact length of the spherical cap until the onset of the sliding motion. Therefore, the roll-off angle of the droplet with volume V and under gravitational acceleration g can be estimated through a horizontal force balance of the tilted surface as [128, 173],

$$\sin\alpha = \frac{l_e\gamma_{\mathrm{LA}}(\cos\theta_R - \cos\theta_A)}{\rho_w V g}. \tag{3.17}$$

The effective length, l_e, depends on the types of surface texture/micro-construct in place. Therefore, the effective pinning length can be described in terms of texture parameter (β), $l_e = 2\pi R_{\mathrm{sl}}\beta$. To be mentioned, McCarthy *et al.* have commented on textured surface stickiness and the importance of pinning force effect on the TCL [174]. It is expected that a micro-structured surface with a smaller texture parameter can have a smaller pinning force, f_P, and hence low CAH, with debatable explanations available in the literature. Although researchers invariably report on self-cleaning textured surfaces with low CAH, it was opined that the pinning force can oppose the smooth motion of TCL and without having a direct relationship with CAH [128].

In the present study, the *Ziziphus* abaxial leaf surface was seen to uphold coexistence of superhydrophobic and superadhesion features, with high enough CAH for all the leaf states. Not surprisingly, the CAH is associated with the pinning of the TCL of the water droplet in contact with the solid surface. It is believed that high CAH may appear due to hydrophilic chemical entities or structural heterogeneity [175–177]. Here, the irregular, nonwoven fibrous abaxial *Ziziphus* leaf surface is seen to exhibit superhydrophobicity and high CAH, possibly due to structural heterogeneity and unique microfiber distribution. Under wetted area, we invoke two scenarios: major area where air–water interface could wet the uppermost microfiber surface resulting in the Cassie (suspended) wetting state. Second, in the minor irregular areas, where the size of air voids may be insufficient to sustain the Laplace pressure balance across the trapped air-water interface, the system would transition to the Wenzel (collapsed) state. To be mentioned, it is the collective response of the nonwoven fibrous surface which accounts for the suspended state and consequently, superhydrophobicity. On the other hand, the high adhesion feature is an add-on feature due to the likelihood of the collapsed wetting state. In fact, when the droplet contact line tends to move with the surface tilting, it may get trapped in the collapsed state at certain irregular micro-textured positions, yielding high CAH and adhesion. The

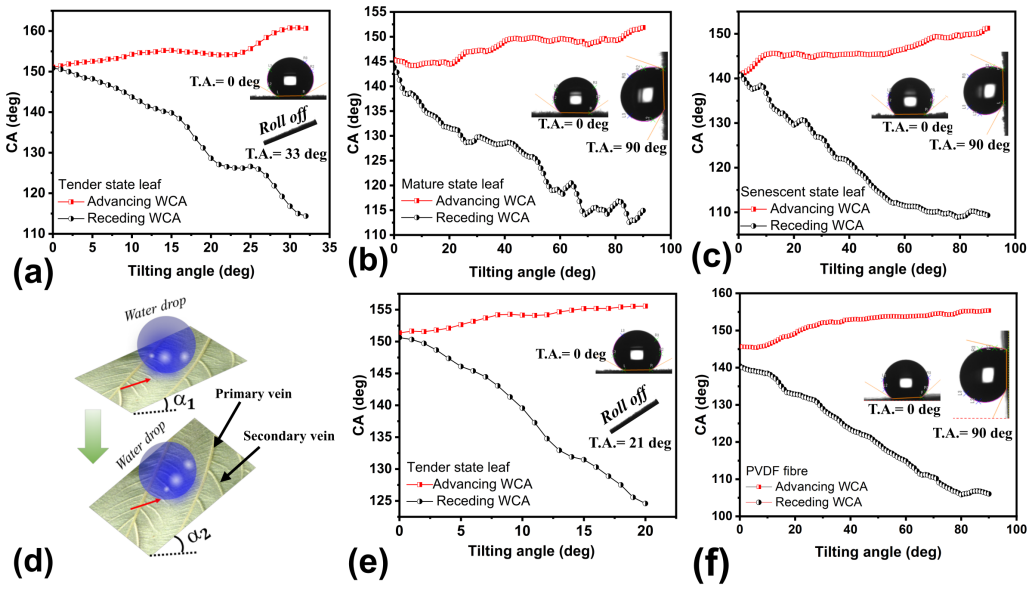

Figure 3.12: The plots show advancing and receding WCA as a function of surface tilting angle: (a) tender state with roll-off angle ~21°, (b) mature state, (c) senescent state, respectively. (d) In the schematic figure, the black arrows represent primary and secondary venation lines on the abaxial leaf surface. The red arrows indicate the leaf venation line, which becomes a barrier for a rolling water droplet when the surface is tilted from $\alpha_1 \rightarrow \alpha_2$°. (e) The tender leaf state with roll-off angle ~33°. (f) The plot for the fabricated PVDF fibrous surface. The insets in the plots depict optical images of the droplet on the surface with a tilting angle (T.A.) of zero degrees and the maximum tilting angle at which the droplet may roll off or remain sticky.

advancing and receding WCA with increasing tilting angle for the abaxial tender, mature, and senescent states of leaves is depicted in Figs. 3.12(a-c, e), respectively. The respective CAH of these states are estimated to be ~30.96°, ~39.3°, and ~42.35°. With the least CAH, the tender leaf experiences a droplet roll-off at a tilting angle of 21° (Fig. 3.12(e)). It is worth noting here that the tender leaf surface could show a range of roll-off angles due to a barrier imposed by the leaf's secondary venation lines that emerge out of the primary veins during dynamic evolution of the droplet with base tilting, shown in Fig. 3.12(d). Consequently, it yields an augmented roll-off angle of ~33° and CAH of ~46.42° (Fig. 3.12(a)). In contrast, the tender leaf surface characterizes a droplet roll-off, whereas other leaf states were extremely sticky, yielding superadhesion features even up to a base tilting angle of 90°. The advancing and receding WCA as a function of tilting angle can be found for the fabricated PVDF fibrous surface that reveal a high CAH of approximately ~49.4°, while water droplet does not roll-off up to a base-tilting of 90° as shown in Fig. 3.12(f) (see Appendix I, Figs. (A.3-A.6).

Interestingly, mature and senescent leaves exhibit relatively better surface adhesion responses as compared to their tender counterpart, possibly to support the evolutionary basis. To be specific, while the tender leaf comes with the highest WCA meant for superhydrophobicity, the mature and senescent states offered higher CAHs

without displaying roll-off and warranting superadhesion response. Thus, the hairy matted surface of *Ziziphus* leaf validates the coexistence and interplay of superhydrophobicity and superadhesion at large.

3.6 Conclusion

- The abaxial leaf of *Ziziphus mauritiana* displays superhydrophobicity and high adhesion due to its hairy, matted surface structure with fiber diameters ranging ~5.6–7.1 μm.
- Water contact angle (WCA) exceeds ~143°, varying by leaf maturity:
  (i) Tender leaf: WCA up to ~151°, roll-off angle ~21°–33°.
  (ii) Mature and senescent leaves: Excellent adhesion, no roll-off at 90° tilt (superadhesion).
- Biomimicking the leaf's structure using PVDF fibers (~4.3 μm diameter) achieved similar superhydrophobicity and high adhesion:
  (i) Grown PVDF fibers: WCA ~145.7°.
  (ii) CAH ~49.4°.
- Nonwoven matted surfaces were effectively modeled using a mathematical WLC model, considering spatial distribution.